

# Determination of thermal expansion, defect formation energy, and defect-induced strain of $\alpha$ -U via *ab initio* molecular dynamics

Benjamin Beeler<sup>1,2,\*</sup>, Khadija Mahbuba<sup>1</sup>, Yuhao Wang<sup>3</sup>, and Andrea Jokisaari<sup>2</sup>

<sup>1</sup>North Carolina State University, Raleigh, NC 27607

<sup>2</sup>Idaho National Laboratory, Idaho Falls, ID 83415

<sup>3</sup>University of Michigan, Ann Arbor, MI 48109

Correspondence\*:

2500 Stinson Dr, Raleigh, NC, 27607

bwbeeler@ncsu.edu

## 2 ABSTRACT

Uranium (U) is often alloyed with molybdenum (Mo) or zirconium (Zr) in order to stabilize its high-temperature body-centered cubic phase for use in nuclear reactors. However, in all metallic fuel forms, the  $\alpha$  phase of U remains in some fraction. This phase decomposition due to temperature or compositional variance can play an outsized role on fuel performance and microstructural evolution. Relatively little is known about fundamental point defect properties in  $\alpha$ -U at non-zero temperatures, from either computational or experimental studies. This work performs the first thorough evaluation of the  $\alpha$  phase of U via *ab initio* molecular dynamics (AIMD). A number of thermophysical properties are calculated as a function of temperature, including equilibrium lattice parameters, thermal expansion, and heat capacity. These results indicate a two-region behavior, with the transition at 400 K. The thermal expansion/contraction in the *a/b* direction occurs rapidly from 100 K up to 400 K, after which a more linear and gradual change in the lattice constant takes place. The volumetric expansion matches experiments quantitatively, but the individual lattice constant expansion only matches experiments qualitatively. Point defect formation energies and induced lattice strains are also determined as a function of temperature, providing insight on defect populations and the fundamentals of irradiation growth in  $\alpha$ -U. Interstitials induce significantly more strain than vacancies, and the nature of that strain is highly dependent on the individual lattice directions. The direction of point defect-induced lattice strain is contrary to the irradiation growth behavior of  $\alpha$ -U. This work shows that isolated point defects cannot be the primary driving force responsible for the significant irradiation-induced growth of  $\alpha$ -U observed experimentally.

**Keywords:** alpha uranium, ab initio molecular dynamics, point defects, lattice strain, fuel swelling

## 1 INTRODUCTION

Uranium (U) is an actinide element exhibiting delocalized f-electrons that exists in three solid phases:  $\alpha$  (face-centered orthorhombic),  $\beta$  (tetragonal with a 30 atom unit cell) and  $\gamma$  (body-centered cubic) Yoo et al. (1998). Below 935 K, U exists in the  $\alpha$  phase Söderlind (1998). Although uranium is alloyed with Mo or Zr in order to stabilize the preferred body-centered cubic phase at lower temperatures, most notably for

nuclear fuel applications, the  $\alpha$  phase persists either in decomposed phase regions (as in the case of U-Mo fuel) or in the low-temperature periphery of the fuel slug (as in the case of U-Zr type fuel). Because of its unique crystal structure,  $\alpha$ -U exhibits anisotropic material properties, for example, thermal expansion Lloyd and Barrett (1966) and elastic constants Fisher and McSkimin (1958). One relevant behavior is the anisotropic irradiation growth of  $\alpha$ -U Leggett et al. (1963), which can lead to the tearing along grain boundaries and the formation of crystallographically aligned pores. These porosities are believed to form due to the interaction of lattice defects and stresses induced by irradiation and a temperature gradient and result in significant volume changes of  $\alpha$ -U Leggett et al. (1963); Paine and Kittel (1958). A full understanding of the relationship between point defects, lattice strains, and the generation of pores, has not been established either experimentally or via computational methods. However, a number of computational studies have been performed into fundamental properties of uranium Jokisaari (2020).

Density functional theory (DFT) is an essential part of computational materials science, addressing a variety of problems in materials design and processing on a fundamental level. Several examinations of U via DFT have been performed on its orthorhombic and body-centered cubic (bcc) structures. Taylor Taylor (2008) used a projector augmented wave (PAW) pseudo-potential to calculate the lattice constants of  $\alpha$ -U and  $\gamma$ -U along with the bulk modulus of both phases and the surface energy of a single surface in  $\alpha$ -U. Xiang, et al. Xiang et al. (2008) also utilized a PAW pseudo-potential to perform an analysis of lattice constants in the  $\alpha$  and  $\gamma$  phases, as well as an analysis of defects in  $\gamma$ -U. Beeler, et al. calculated the lattice constants and elastic constants of  $\alpha$ ,  $\beta$  and  $\gamma$ -U Beeler et al. (2013), in addition to the point defect properties in both  $\alpha$  and  $\gamma$ -U Beeler et al. (2010). Huang and Wirth Huang and Wirth (2011, 2012) calculated intrinsic and extrinsic point defect formation energies and migration barriers in  $\alpha$ -U. These DFT investigations showed a general, if imperfect, agreement with the experimental bulk moduli, lattice and elastic constants, and vacancy formation energy Yoo et al. (1998); Barrett et al. (1963); Matter et al. (1980).

Key areas lacking from the DFT-based literature on  $\alpha$ -U include an analysis of temperature-dependent bulk properties, including thermal expansion and heat capacity, and temperature-dependent defect properties. Extrapolation of 0 K properties to compare to elevated temperature experiments can be ill-advised, particularly for complex crystal structures or for point defects. However, *ab initio* molecular dynamics (AIMD) allows for quantum mechanical-based calculations to be performed at non-zero temperatures. AIMD has been utilized to study a variety of systems including liquid phase diffusion in Al-Si Manga and Poirier (2018), the adsorption energy of Fe on TiN surfaces Wang et al. (2010), NaCl dissolution in water Timko et al. (2010) and finite temperature phonon dispersion curves in bcc Zr and bcc Li Hellman et al. (2011). Hood, et al. Hood et al. (2008) have previously utilized AIMD to study the equation of state of U and the variation in density of states for the liquid phase of U at two unique temperatures. Hood, et al. utilized a unique pseudo-potential that was presented in that same manuscript Hood et al. (2008). Soderlind, et al. Söderlind et al. (2012) utilized self-consistent *ab initio* lattice dynamics (SCAILD) to study the high-temperature stabilization of the  $\gamma$ -U phase by calculating phonon modes at 1100 K. There have been several investigations of the free energy via the temperature-dependent effective potential (TDEP) technique Hellman et al. (2013); Ladygin et al. (2020); Kruglov et al. (2019); Bouchet and Bottin (2017); Castellano et al. (2020), and one recent AIMD investigation into the defect formation energies in  $\gamma$ -U at high temperatures Beeler et al. (2020). Despite numerous investigations into metallic uranium, AIMD has not been deployed to study temperature-dependent properties of  $\alpha$ -U, such as thermal expansion or defect formation energies.

In this work, AIMD simulations are performed to calculate the equilibrium volume of  $\alpha$ -U as a function of temperature. Utilizing these equilibrium volumes, the three lattice constants of  $\alpha$ -U are determined, yielding

anisotropic thermal expansion calculations. Additionally, point defect formation energies for interstitials and vacancies are calculated as a function of temperature. The lattice strain from the introduction of these point defects is calculated, providing insight into the fundamental stages of irradiation growth. This is the first AIMD investigation of point defects in  $\alpha$ -U.

## 2 MATERIALS AND METHODS

Systems are investigated using the Vienna *ab initio* Simulation Package (VASP) Kresse and Hafner (1993, 1994); Kresse and Fürthmüller (1996a,b). The projector augmented wave (PAW) method Blöchl (1994); Kresse and Joubert (1999) is utilized within the density functional theory Hohenberg and Kohn (1964); Kohn and Sham (1965) framework. Calculations are performed using the Perdew-Burke-Ernzerhof (PBE) Perdew et al. (1996, 1997) generalized gradient approximation (GGA) density functional implementation for the description of the exchange-correlation. A uranium PAW pseudo-potential with the  $6s^2 6p^6 5f^3 6d^1 7s^2$  valence electronic configuration and a core represented by [Xe, 5d, 4f] is utilized. Methfessel and Paxton's smearing method Methfessel and Paxton (1989) of the first order is used with a width of 0.1 eV to determine the partial occupancies for each wavefunction. A Monkhorst-Pack Monkhorst and Pack (1976)  $1 \times 1 \times 1$  k-point mesh was utilized for Brillouin zone sampling. Uranium is assumed to be non-magnetic, in accordance with both experiments Lide (2000) and previous simulations Beeler et al. (2013), and as such calculations are non-spin-polarized. The Hubbard U term is not applied to the *f* electrons, in accordance with previous computational studies that utilized DFT on  $\alpha$ -U Huang and Wirth (2011, 2012); Taylor (2008); Beeler et al. (2013). The precision is set to normal and the energy cutoff is increased to 300 eV. The electronic self-consistent loop exit criterion is set to  $10^{-4}$  and the precision for projectors in real space is increased to  $-10^{-4}$ . A 180 atom supercell ( $5 \times 3 \times 3$  unit cells) is utilized for all simulations. Such a supercell is sufficiently large to preclude defect-defect interactions Huang and Wirth (2011). Dynamics were carried out in the NpT ensemble with Parinello-Rahman dynamics and a Langevin thermostat to control temperature. The temperature range investigated is from 100 K to 800 K, in increments of 100 K, to span nearly the entire range of stability of the  $\alpha$  phase of U. The Langevin friction coefficient for both the atomic and lattice degrees-of-freedom was set to  $5 \text{ ps}^{-1}$ , with a fictitious mass for the lattice degrees of freedom of 500 amu. The timestep is set to 2.0 fs, and the initial structures are equilibrated at the target temperature for 8 ps. The trajectories of the total supercell energy, pressure, and individual lattice vectors are analyzed as a function of timestep to ensure that an equilibrated state has been reached and each of these quantities is oscillating around a given value, with the pressure oscillating around zero. Subsequently, the simulations are further equilibrated for 2000 timesteps (4 ps) for the determination of equilibrium properties. In order to obtain average properties over the *ab initio* molecular dynamics simulation, the energies and lattice constants for the final 1500 timesteps (3 ps) are extracted and averaged. To ensure statistical significance of the results, ten unique simulations are performed for each simulation setup. An example trajectory of the individual supercell lattice constants as a function of time at 300 K is shown in Fig. 1. The standard deviation in the *a*, *b*, and *c* equilibrium lattice constants from this single simulation are 0.01 Å, 0.02 Å and 0.01 Å, respectively. It should be emphasized that this was a single simulation, and ten such simulations were performed to obtain the averaged equilibrium structures and energies. Error bars are excluded from figures in the results that pertain to lattice constants, due to the small deviations observed in the dataset.

The thermal expansion is calculated both for individual lattice constants, and as a volume averaged value, via equation 1:

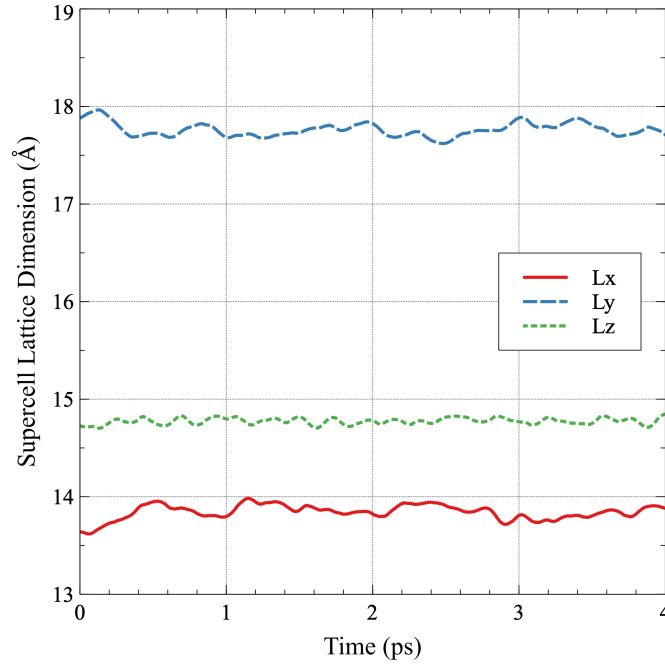


**Figure 1.** The supercell lattice dimensions as a function of time for  $\alpha$ -U. Each dimension is averaged over the final 3 ps to obtain the average lattice constant in the simulation.

$$\alpha = \frac{L - L_0}{L_0} \quad (1)$$

113 where  $\alpha$  is the thermal expansion, and  $L$  is the length of the individual lattice constant or averaged lattice  
 114 constant (cube root of the volume) at a given temperature, and  $L_0$  is the reference length at a given  
 115 temperature. The formation energy of point defects is calculated via equation 2:

$$E_f = E^* - \frac{n \pm 1}{n} \times E_0 \quad (2)$$

116 where  $E^*$  is the energy of a system with a defect (with  $n \pm 1$  atoms),  $n$  is the number of atoms in the  
 117 defect-free system and  $E_0$  is the energy of a defect-free system with  $n$  atoms. Equation 2 utilizes  $(n + 1)$  for  
 118 interstitials and  $(n - 1)$  for vacancies. The molar heat capacity is determined from equation 3:

$$C_P = \left( \frac{\delta H}{\delta T} \right)_P \quad (3)$$

119 where  $H$  is the enthalpy (potential plus kinetic energy),  $T$  is the temperature, and it is emphasized that this  
 120 is determined for a constant pressure, which in these simulations is zero pressure. The total heat capacity is  
 121 a sum of the lattice (Eq. 3) and the electronic components of the heat capacity. The electronic heat capacity  
 122 coefficient ( $\gamma_e$ , where the electronic heat capacity is  $\gamma_e \times T$ ) has been experimentally reported to be 10.12  
 123 mJ/mol-K<sup>2</sup> Marchidan and Ciopec (1976); Schachinger and Lamprecht (1989) , and this value is utilized  
 124 here to determine the total heat capacity as a function of temperature.

### 3 RESULTS

#### 3.1 Equilibrium properties of $\alpha$ -U

The equilibrium lattice constants at 300 K were calculated to be:  $a = 2.78 \text{ \AA}$ ,  $b = 5.91 \text{ \AA}$ , and  $c = 4.93 \text{ \AA}$ . These results compare very favorably to the experimental literature ( $a = 2.85 \text{ \AA}$ ,  $b = 5.87 \text{ \AA}$ , and  $c = 4.96 \text{ \AA}$  Lawson et al. (1988)), with the largest deviation observed for the  $a$  lattice constant at a magnitude of approximately 2.5%. Some deviation is not unexpected, as it has been shown that DFT calculations do not always exactly match the experimental findings, particularly for the lattice constant. However, these results are in accordance with previously computational investigations of  $\alpha$ -U performed at 0 K, when thermal expansion is taken into account Huang and Wirth (2011); Beeler et al. (2013). The complete data for equilibrium lattice constants as calculated in this work is included in Table A1.

The normalized lattice constants as a function of temperature are shown in Fig. 2. Each lattice constant is normalized to its determined value at 100 K, which is the lowest temperature analyzed. Thermal expansion occurs in both the  $a$  and  $c$  directions, while thermal contraction occurs in the  $b$  direction, as has been previously experimentally observed Touloukian et al. (1975). The recommended directional linear thermal expansion curves from Touloukian et al. (1975) are included as a comparison in Fig. 3. Touloukian summarized 48 individual experiments on both single and polycrystalline samples and provided a recommended tabular fit for each  $a$ ,  $b$ ,  $c$ , and volumetric thermal expansion. These experiments did not all necessarily quantify their uncertainty, however, Touloukian stated that the recommended values are considered accurate to within  $\pm 5\%$ . The data in Fig. 3 utilizes 300 K as the reference point for both the AIMD data and the experimental data, and as such, the change in length at 300 K is zero. It can be observed that the AIMD predicted thermal expansion in the  $a$  direction is significantly greater than that determined from experiment. Similarly, the amount of contraction in the  $b$  direction predicted from AIMD is significantly greater than that observed in experiments. However, the  $c$  direction exactly matches the linear thermal expansion determined from experiments. Qualitatively, all of the behaviors are identical, with the  $a$  and  $b$  directions expressing a more extreme expansion/contraction behavior. The source of the deviations from experiment is currently unknown. A comparison of the elastic constants calculated at 0 K Beeler et al. (2013) compared to the experimentally determined elastic constants Fisher and McSkimin (1958) yielded no obvious discrepancies that would point to the specific observed trends in the thermal expansion as a function of temperature. The DFT-predicted elastic constants generally overestimate the experimental elastic constants, including all of  $C_{11}$ ,  $C_{22}$ ,  $C_{33}$ , and the bulk modulus, and do not imply the existence of exaggerated swelling/contraction in the  $a/b$  directions.

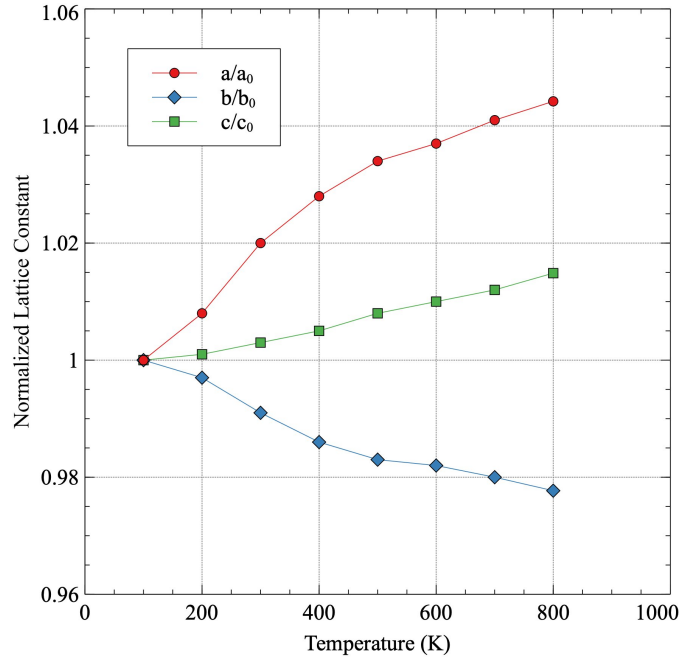


**Figure 2.** The normalized lattice constants as a function of temperature for  $\alpha$ -U. Each lattice constant is normalized to its value at 100 K.

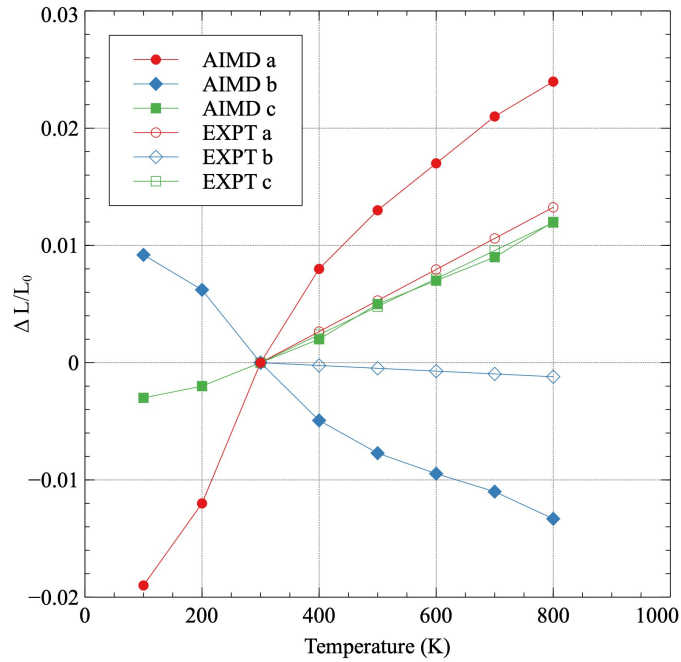


**Figure 3.** The linear thermal expansion coefficient for each lattice constant in  $\alpha$ -U. Thermal expansion is normalized to 300 K, which is the lowest temperature in the experimental data Touloukian et al. (1975).

155 The volume-averaged linear thermal expansion is calculated and compared to a different set of  
 156 experimental results from Touloukian Touloukian et al. (1975) in Fig. 4. The volume-averaged linear  
 157 thermal expansion utilizes the cube-root of the volume at each temperature of interest. Interestingly, the  
 158 data from AIMD nearly exactly matches the experimental results for volumetric-averaged linear thermal  
 159 expansion, with only slight deviations presenting above 600 K. Thus, despite the differences in the



individual components of thermal expansion in  $\alpha$ -U, which are somewhat substantial, the cumulative effect on total volume expansion reproduces the experimental observations.

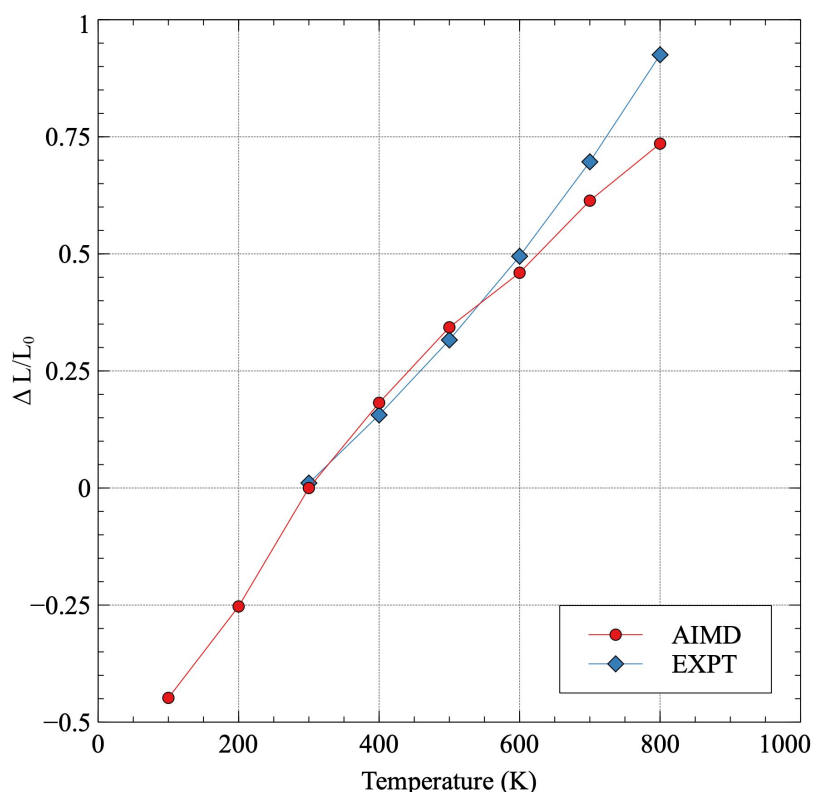


**Figure 4.** Volume-averaged linear thermal expansion in  $\alpha$ -U. Thermal expansion is taken with respect to 300 K and compared to experimental results Touloukian et al. (1975).

The total constant pressure heat capacity is determined from a summation of equation 3 and the electronic heat capacity contribution as determined by experiments, and is plotted in Fig. 5. The complete heat capacity data as calculated in this work is included in Table A2. Data points are shown at intermediate temperatures, as the formalism in equation 3 assumes effectively a constant value of  $C_p$  over the temperature range. Thus, utilizing data points at 100 K and 200 K, for example, yields a value of  $C_p$  at 150 K in this work. Experimental data is only reported for room temperature and upwards, and the agreement with the AIMD is generally excellent. The maximum deviation is observed at 750 K, where the AIMD results under-predict the magnitude of  $C_p$  by approximately 11%. At lower temperatures, the deviation can be less than 5%. Thus, while the magnitude of the heat capacity is generally the same, it appears that the experimentally observed heat capacity is more sensitive to temperature, showing a total change from 250-750 K of 17 J/mol-K, while AIMD only predicts an increase of 11 J/mol-K over this temperature range. Sources of error between the experimental measurements and computational calculations can include impurities in the material, effects from underlying microstructure, defect concentrations, inaccuracies in the fundamental computational theories, etc. Thus, while there is not exact agreement over the entire temperature range, the correlation between the AIMD results and experiment is considered quite good.

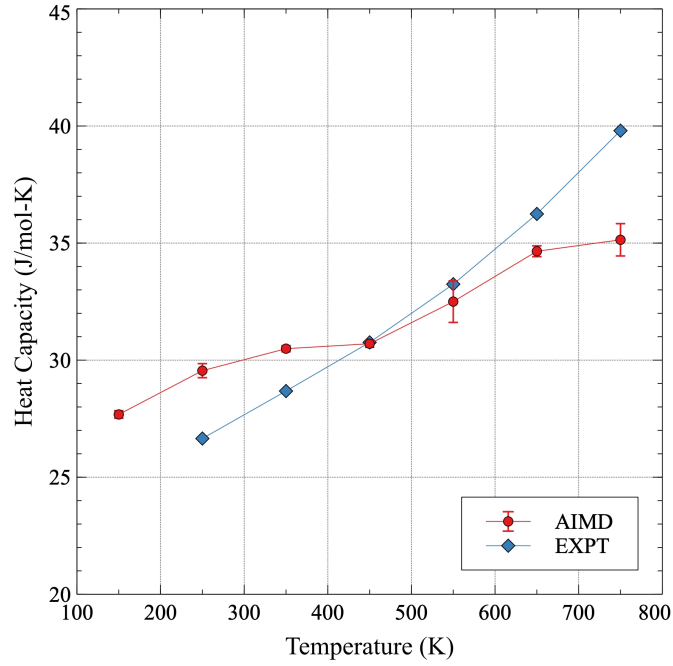


**Figure 5.** The constant pressure heat capacity of  $\alpha$ -U from 100 K to 800 K. Results from this work are compared to experimental results from Konings Konings and Benes (2010). Error bars indicate twice the standard error of the AIMD dataset.

### 3.2 Point defects in $\alpha$ -U

The point defect formation energy of interstitials and vacancies in  $\alpha$ -U is shown in Fig. 6 and included in Table A3. The defect formation energy for both types of defects tends to slightly decrease with increasing temperature until approximately 400 K. Above 400 K, an increase in the defect formation energy with increasing temperature is observed. The relative magnitudes of the defect formation energies with respect to one another are near-constant across the entire temperature range investigated, with the average interstitial formation energy (3.4 eV) about 2.3 times the average vacancy formation energy (1.46 eV). Error bars shown in Fig. 6 are twice the standard error, where the standard error for formation energies is defined as

$$SE = \sqrt{\frac{\sigma_{bulk}}{\sqrt{N}} + \frac{\sigma_{def}}{\sqrt{N}}} \quad (4)$$

where  $\sigma_{bulk/def}$  is the standard deviation of the dataset utilized for determining the average energies of either the defect-free or the defected system, and  $N$  is the sample size, which is ten simulations for both the defected and defect-free simulations. The standard error in the data set tends to increase with increasing temperature, as would be expected. The results from the lower temperature regime can be compared to previous results from 0 K DFT calculations. At 100 K, the interstitial formation energy is found to be 3.81 eV, and the vacancy formation energy is found to be 1.69 eV. These results compare favorably to previous 0 K DFT results Huang and Wirth (2011), which showed a vacancy formation energy of 1.69 eV (an exact match), and interstitial formation energy of 4.42 eV. That the interstitial formation energy from this work is lower is not unsurprising. While DFT can access any prescribed positional state, the identification of the lowest energy defect location can often be complex and is complicated by the possibility of local minima. By including temperature effects, atomic vibrations can more readily overcome any potential local minima that exist within the energy surface, theoretically finding the lowest possible energy state, and



197 thus the equilibrium defect location at that given temperature. This data can be utilized to conduct higher  
 198 length scale simulations that attempt to describe defect formation and mobility and those which include an  
 199 estimation of the equilibrium concentrations of defects.

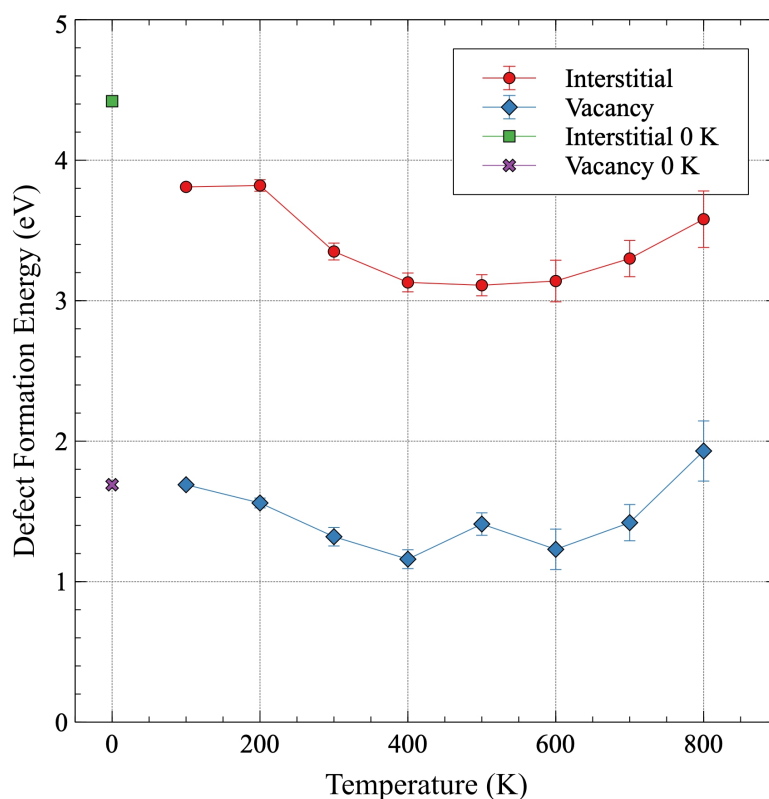


**Figure 6.** The formation energy of an interstitial and a vacancy in  $\alpha$ -U as a function of temperature. The defect formation energies from previous DFT work are included for comparison Huang and Wirth (2011).

200 The introduction of a defect and relaxation in an NpT ensemble allows for the analysis of volume changes  
 201 due to individual point defects. These volume changes are reported as a function of temperature in Fig.  
 202 7, with error bars included as twice the standard deviation of the dataset. The defect-induced strains are  
 203 also included in Table A4. For interstitials, there exist two distinct regimes in the defect-induced strain  
 204 environment, with 400 K serving as the demarcation temperature. Below 400 K, strain is relatively large  
 205 and positive (lattice expansion) in the  $a$  direction, and relatively large and negative (lattice compression)  
 206 for the  $b$  direction. The magnitudes of those strains decrease with increasing temperature up to 400 K,  
 207 above which they maintain a relatively fixed value, with some statistical fluctuation. It is unknown whether  
 208 the deviation at 600 K is due to some distinct behavioral changes, or is simply the result of thermal noise.  
 209 However, data points at 600 K generally remain within the general trend of the dataset. The  $c$  lattice  
 210 constant exhibits very slight positive strain across the entire temperature range, with no obvious changes  
 211 in behavior. For vacancies, the general magnitude of the strain is significantly less than that observed  
 212 for interstitials, with the maximum strain of -0.5% observed at 800 K for the  $b$  lattice constant. While  
 213 it is more difficult to discern trends in the vacancy strain as a function of temperature, several pieces of  
 214 information can be readily extracted. The  $c$  lattice constant displays no observed strain from vacancies at  
 215 any temperature. For the  $a$  and  $b$  lattice constants, opposite trends present themselves above 400 K, in that  
 216 the  $a$  lattice constant strain increases with increasing temperature and the  $b$  lattice constant strain decreases  
 217 with increasing temperature. In a general sense, the strain behavior of defects is as expected, in that

interstitials yield a lattice expansion, while vacancies produce lattice contraction. However, the manner in which those volumetric averages are produced is quite complex and is significantly temperature-dependent.

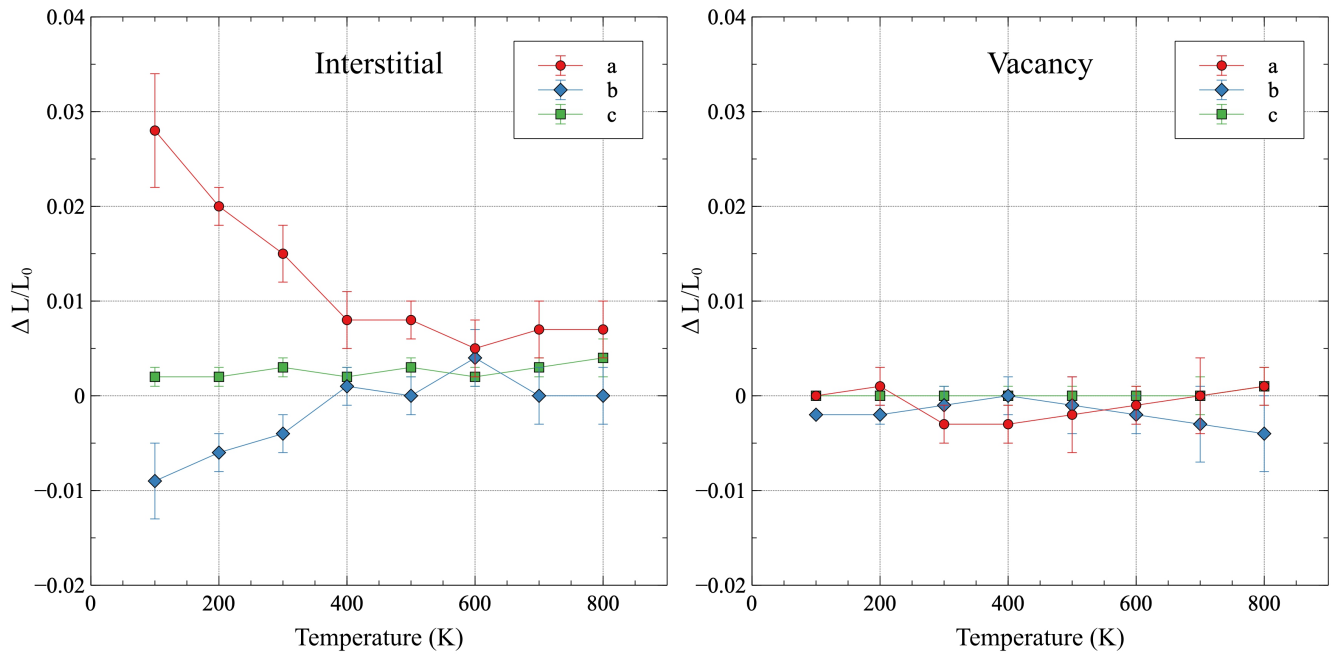


**Figure 7.** The lattice strain induced from an interstitial or vacancy in  $\alpha$ -U as a function of temperature, taken with respect to the equilibrium volume at that given temperature. Error bars indicate twice the standard deviation of the dataset.

## 4 DISCUSSION

This work indicates several lattice and volume effects that are strongly dependent upon the temperature of the system. Excepting the heat capacity, all of these calculated properties seem to indicate two regions of behavior, one below 400 K and one above 400 K. Also, it should be re-emphasized that the heat capacity utilized an experimental data point for the determination of the electronic heat capacity. Thus, from the purely computationally obtained data, there are differences in lattice constant, defect-induced lattice strain, and defect formation energy, in these two temperature regimes. To briefly summarize, thermal expansion/contraction in the  $a/b$  direction occurs rapidly from 100 K up to 400 K, after which a more linear and gradual change in the lattice constant takes place. Defect formation energies decrease in magnitude up to 400 K, above which they tend to slightly increase. Defect lattice strains for interstitials decrease/increase in the  $a/b$  direction up to 400 K, above which they maintain essentially the same magnitude. A similar trend in defect lattice strains for vacancies is present, but the magnitude is significantly less and potentially swamped by thermal fluctuations, and thus the statistical certainty of the finding is reduced.

In an attempt to identify underlying changes in the atomic and electronic structure as a function of temperature, two additional analyses were performed. The first was a coordination analysis, in which the radial distribution function (rdf) was constructed for a snapshot of the equilibrated  $\alpha$ -U structure at 100 K, 400 K, and 800 K. If a modification in the bond lengths is occurring that can yield differences in structure, such a modification would present itself as peak shifts in the rdf. This coordination analysis is presented in Fig. 8, but yielded no discernible trends, and the general bond length and peak broadening confirm what is observed in Fig. 2 and Fig. 3 outlining thermal expansion. Specifically, there is general peak broadening

with temperature, and the second nearest neighbor peak (in the  $b$  direction) slightly shifts towards a smaller distance. The second analysis involved the electronic density of states (DOS). If the character of valence electrons participating in the bonding is changing as a function of temperature, the electronic DOS would identify such changes, and the electronic DOS is known to slightly change as a function of the phase of uranium Beeler et al. (2013). The electronic DOS was calculated, and only minimal variation in the electronic structure was observed as a function of temperature. There was no indication that two regions of electronic structure behavior exist for the  $\alpha$  phase. Due to the lack of identifiable structure variation as a function of temperature, likely due to statistical noise in the sampling. These results are not displayed here, as the DOS can be obtained from the literature Beeler et al. (2013); Hood et al. (2008). The underlying cause of the apparent two-region behavior is unclear and warrants further computational investigation, in addition to experimental studies on high-purity uranium to either confirm or refute the findings in this work. It should be emphasized that these results are statistically significant, but are still susceptible to inherent errors in the modeling methodology, such as the inability for DFT to predict the lattice and elastic constants of  $\alpha$ -U with sufficient accuracy at 0 K.

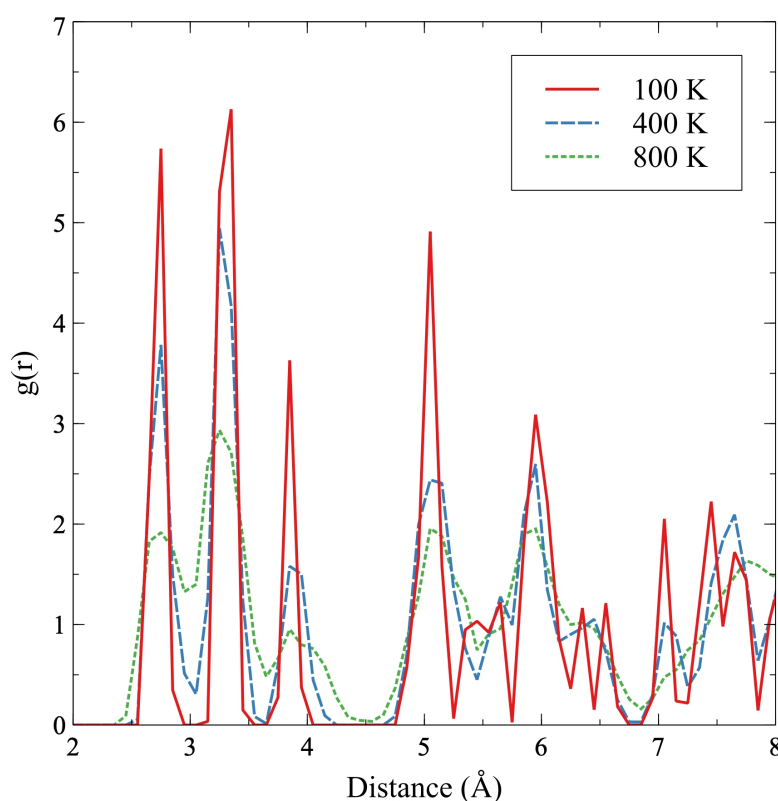


**Figure 8.** The radial distribution function in  $\alpha$ -U at 100 K, 400 K, and 800 K.

This work has identified that individual point defects can produce somewhat significant lattice strain, but it is unknown if such point defects could be responsible for experimentally observed macroscopic shape change. Comparison of the calculated direction of the defect-induced strains to the experimental literature on irradiation growth provides contradictory information. Paine and Kittel Paine and Kittel (1958) and Loomis and Gerber Loomis and Gerber (1968) both investigated dimensional change of single-crystal uranium under irradiation. Their findings were in general agreement with one another, and showed a contraction of the bulk crystal in the  $a$  direction, an expansion in the  $b$  direction, and no change in the  $c$

direction. While the AIMD results of point defect-induced strains presented here agree with the lack of dimensional change in the  $c$  direction, exactly the opposite behavior is observed in Fig. 7 for the  $a$  and  $b$  directions. This work showed that interstitials are the dominant strain inducers, producing expansion in the  $a$  direction and contraction in the  $b$  direction. Due to the relatively large induced strains from interstitials, it is expected that these types of point defects would display strongly anisotropic diffusion. Given that isolated point defects lead to the opposite trends from those observed experimentally, it is possible that defect clusters or defect loops display different strain behaviors than individual point defects, and are the features responsible for irradiation growth in  $\alpha$ -U. Such research is beyond the scope of AIMD, which is currently sufficiently computationally expensive to exclude the possibility of analysis of extended defects. Thus, classical molecular dynamics simulations can be performed and validated against the work presented here. Ideally, in addition to further computational studies, the experimental results from over sixty years ago should be reproduced and modern characterization methods applied to extract fundamental defect populations, densities, and orientations.

## 5 CONCLUSIONS

In this study, AIMD simulations were performed to calculate temperature-dependent properties of the  $\alpha$  phase of U from 100 K to 800 K. The thermal expansion of each lattice constant was analyzed and compared to the experimental literature. Although the general direction of thermal expansion corresponded to the experimental findings (positive in  $a$  and  $c$ , negative in  $b$ ), the magnitudes of coefficient of thermal expansion for the  $a$  and  $b$  directions was greater than that observed experimentally. However, the volumetric expansion corresponded nearly exactly to the experimental findings in the literature. The heat capacity was calculated as a function of temperature and showed a general agreement with experimental results, although the computationally determined heat capacity was slightly less sensitive to temperature. Variation in point defect formation energies was determined, with an average interstitial formation energy of 3.40 eV, and an average vacancy formation energy of 1.46 eV, over the entire temperature range. Lattice strains resulting from point defects were determined, showing that interstitials induce significantly more strain than vacancies, and the nature of that strain is highly dependent on the individual lattice directions, where the  $a$  direction expands and the  $b$  contracts due to the introduction of an interstitial. Finally, all of these results seem to indicate a two-region behavior, with the transition at 400 K. The thermal expansion/contraction in the  $a/b$  direction occurs rapidly from 100 K up to 400 K, after which a more linear and gradual change in the lattice constant takes place. Defect formation energies decrease in magnitude up to 400 K, above which they tend to slightly increase. Defect lattice strains for interstitials decrease/increase in the  $a/b$  direction up to 400 K, above which they maintain essentially the same magnitude. Coordination and electronic structure investigations provided no insight into the possible cause of this potential transition in behavior.

This work has shown that isolated point defects cannot be the primary driving force responsible for the significant irradiation-induced growth of  $\alpha$ -U observed experimentally. This work can be utilized as the basis for mesoscale simulations that take into account defect populations, defect diffusion, and defect strain behaviors. It is emphasized that additional computational work utilizing classical molecular dynamics on extended defects should be performed, in addition to experimental irradiation and characterization, to further elucidate the underlying phenomena governing the interactions of point defects with the  $\alpha$ -U crystal structure.

### 5.0.1 Permission to Reuse and Copyright

Figures, tables, and images will be published under a Creative Commons CC-BY license and permission must be obtained for use of copyrighted material from other sources (including republished/adapted/modified/partial figures and images from the internet). It is the responsibility of the

303 authors to acquire the licenses, to follow any citation instructions requested by third-party rights holders,  
304 and cover any supplementary charges.

CONFLICT OF INTEREST STATEMENT

305 This study received funding from Battelle Energy Alliance, LLC. The funder was not involved in the study  
306 design, collection, analysis, interpretation of data, the writing of this article or the decision to submit it  
307 for publication. The authors declare that the research was conducted in the absence of any commercial or  
308 financial relationships that could be construed as a potential conflict of interest.

AUTHOR CONTRIBUTIONS

ACKNOWLEDGMENTS

309 This work is supported through the INL Laboratory Directed Research and Development (LDRD) Program  
310 under DOE Idaho Operations Office Contract DE-AC07-05ID14517. This manuscript has been authored  
311 by Battelle Energy Alliance, LLC with the U.S. Department of Energy. The publisher, by accepting the  
312 article for publication, acknowledges that the U.S. Government retains a nonexclusive, paid-up, irrevocable,  
313 worldwide license to publish or reproduce the published form of this manuscript, or allow others to do so, for  
314 U.S. Government purposes. This research made use of the resources of the High-Performance Computing  
315 Center at Idaho National Laboratory, which is supported by the Office of Nuclear Energy of the U.S.  
316 Department of Energy and the Nuclear Science User Facilities under Contract No. DE-AC07-05ID14517.

6 APPENDIX

317 This appendix includes tabulated data which has been presented and discussed above.

Table A1. The calculated lattice parameter of  $\alpha$ -U from 100 K to 800 K.

Temperature (K)	$a_0$ (Å)	$b_0$ (Å)	$c_0$ (Å)	$V/at$ (Å <sup>3</sup> )
100	2.72	5.96	4.91	79.75
200	2.74	5.94	4.92	80.22
300	2.78	5.91	4.93	80.83
400	2.80	5.88	4.94	81.27
500	2.82	5.86	4.95	81.67
600	2.82	5.85	4.96	81.95
700	2.83	5.84	4.97	82.33
800	2.84	5.83	4.98	82.63

Table A2. The calculated constant pressure heat capacity of  $\alpha$ -U from 100 K to 800 K, compared to experimental values from Konings and Benes (2010). Units in J/mol-K.

Temperature (K)	AIMD	Reference
150	27.7	-
250	29.5	26.7
350	30.5	28.7
450	30.7	30.8
550	32.5	33.2
650	34.7	36.2
750	35.1	39.8

**Table A3.** The interstitial and vacancy formation energy in  $\alpha$ -U as a function of temperature. AIMD results are compared to 0 K DFT data (denoted with \*) from Huang and Wirth (2011). Units in eV.

Temperature (K)	Interstitial	Vacancy
0*	4.42	1.69
100	3.81	1.69
200	3.82	1.56
300	3.35	1.32
400	3.13	1.16
500	3.11	1.41
600	3.14	1.23
700	3.30	1.42
800	3.58	1.93

**Table A4.** The defect-induced strain from interstitials and vacancies as a function of temperature. The strain is defined as  $\Delta L/L_0$ , where  $L_0$  is the reference length at the given temperature.

Temperature (K)	Interstitial			Vacancy		
	a	b	c	a	b	c
100	0.028	-0.009	0.002	0.000	-0.002	0.000
200	0.020	-0.006	0.002	0.001	-0.002	0.000
300	0.015	-0.004	0.003	-0.003	-0.001	0.000
400	0.008	0.001	0.002	-0.003	0.000	0.000
500	0.008	0.000	0.003	-0.002	-0.001	0.000
600	0.005	0.004	0.002	-0.001	-0.002	0.000
700	0.007	0.000	0.003	0.000	-0.003	0.000
800	0.007	0.000	0.004	0.001	-0.004	0.001

## REFERENCES

- Barrett, C., Mueller, H., and Hitterman, R. (1963). Crystal structure variations in alpha uranium at low temperatures. *Phys. Rev.* 129, 625
- Beeler, B., Andersson, D., Jiang, C., and Zhang, Y. (2020). Ab initio molecular dynamics investigation of point defects in gamma-u. *J. Nucl. Mater.* 545, 152415
- Beeler, B., Deo, C., Baskes, M., and Okuniewski, M. (2013). First principles calculations of the structure and elastic constants of alpha, beta and gamma uranium. *J. Nucl. Mater.* 433, 143
- Beeler, B., Good, B., Rashkeev, S., Deo, C., Baskes, M., and Okuniewski, M. (2010). First principles calculations for defects in U. *J. Phys.: Cond. Mat.* 22, 505703
- Blöchl, P. (1994). Projector augmented-wave method. *Phys. Rev. B* 50, 17953
- Bouchet, J. and Bottin, F. (2017). High-temperature and high-pressure phase transitions in uranium. *Phys. Rev. B* 95, 054113
- Castellano, A., Bottin, F., Dorado, B., and Bouchet, J. (2020). Thermodynamic stabilization of  $\gamma$ -u-mo alloys: Effect of mo content and temperature. *Phys. Rev. B* 101, 184111
- Fisher, E. and McSkimin, H. (1958). Adiabatic elastic moduli of single crystal alpha uranium. *J. Appl. Phys.* 29, 1473
- Hellman, O., Abrikosov, I. A., and Simak, S. I. (2011). Lattice dynamics of anharmonic solids from first principles. *Phys. Rev. B* 84, 180301(R)
- Hellman, O., Steneteg, P., Abrikosov, I., and Simak, S. (2013). Temperature dependent effective potential method for accurate free energy calculations of solids. *Phys. Rev. B* 87, 104111



- 337 Hohenberg, P. and Kohn, W. (1964). Inhomogeneous electron gas. *Phys. Rev.* 136, B864
- 338 Hood, R., Yang, L., and Moriarty, J. (2008). Quantum molecular dynamics simulations of uranium at high  
339 pressure and temperature. *Phys. Rev. B* 78, 024116
- 340 Huang, G.-Y. and Wirth, B. (2011). First-principles study of diffusion of interstitial and vacancy in alpha  
341 U-Zr. *J. Phys.: Cond. Mat.* 23, 205402
- 342 Huang, G.-Y. and Wirth, B. (2012). First-principles study of bubble nucleation and growth behaviors in  
343 alpha u-zr. *J. Phys.: Cond. Mat.* 24, 415404
- 344 Jokisaari, A. (2020). Irradiation-induced internal stresses in polycrystalline alpha-uranium: a mesoscale  
345 mechanical approach. *Comp. Mat. Sci.* 176, 109545
- 346 Kohn, W. and Sham, L. (1965). Self-consistent equations including exchange and correlation effects. *Phys.*  
347 *Rev.* 140, A1133
- 348 Konings, R. and Benes, O. (2010). The thermodynamic properties of the f-elements and their compounds.  
349 i. the lanthanide and actinide metals. *Journal of Physical and Chemical Reference Data* 39, 043102
- 350 Kresse, G. and Fürthmüller, J. (1996a). Efficiency of ab-initio total energy calculations for metals and  
351 semiconductors using a plane-wave basis set. *Comput. Mat. Sci.* 6, 15
- 352 Kresse, G. and Fürthmüller, J. (1996b). Efficient iterative schemes for ab initio total-energy calculations  
353 using a plane-wave basis set. *Phys. Rev. B* 54, 11169
- 354 Kresse, G. and Hafner, J. (1993). Ab initio molecular dynamics for liquid metals. *Phys. Rev. B* 47, 558
- 355 Kresse, G. and Hafner, J. (1994). Ab initio molecular-dynamics simulation of the liquid-metal-amorphous-  
356 semiconductor transition in germanium. *Phys. Rev. B* 49, 14251
- 357 Kresse, G. and Joubert, D. (1999). From ultrasoft pseudopotentials to the projector augmented-wave  
358 method. *Phys. Rev. B* 59, 1758
- 359 Kruglov, I., Yanilkin, A., Oganov, A., and Korotaev, P. (2019). Phase diagram of uranium from ab initio  
360 calculations and machine learning. *Phys. Rev. B* 100, 174104
- 361 Ladygin, V., Korotaev, P., Yanilkin, A., and Shapeev, A. (2020). Lattice dynamics simulation using machine  
362 learning interatomic potentials. *Comp. Mat. Sci.* 172, 109333
- 363 Lawson, A., Olsen, C., Richardson, J., Mueller, M., and Lander, G. (1988). Structure of beta-uranium.  
364 *Acta Cryst.* B44, 89
- 365 Leggett, R., Bierlein, T., and Mastel, B. (1963). *Irradiation behavior of high purity uranium*. Tech. Rep.  
366 HW-79559, Hanford Laboratories
- 367 Lide, D. (2000). *Handbook of Chemistry and Physics: A Ready-Reference Book Chemical and Physical*  
368 *Data* (CRC-Press)
- 369 Lloyd, L. and Barrett, C. (1966). Thermal expansion of alpha uranium,. *J. Nucl. Mater.* 18, 55
- 370 Loomis, B. and Gerber, S. (1968). Length and electrical resistivity changes of neutron irradiated uranium.  
371 *Phil. Mag.* 18, 539
- 372 Manga, V. and Poirier, D. (2018). Ab initio molecular dynamics simulation of self-diffusion in al-si binary  
373 melts. *Modelling Simul. Mater. Sci. Eng.* 26, 065006
- 374 Marchidan, D. and Ciopec, M. (1976). Enthalpy of uranium to 1500 k by drop calorimetry. *J. Chem.*  
375 *Thermo.* 8, 691
- 376 Matter, H., Winter, J., and Triftshauser, W. (1980). Investigation of vacancy formation and phase  
377 transformations in uranium by positron annihilation. *J. Nucl. Mater.* 88, 273
- 378 Methfessel, M. and Paxton, A. (1989). High-precision sampling for brillouin-zone integration in metals.  
379 *Phys. Rev. B* 40, 3616
- 380 Monkhorst, H. and Pack, J. (1976). Special points for brillouin-zone integrations. *Phys. Rev. B* 13, 5188

- 381 Paine, S. and Kittel, J. (1958). *PRELIMINARY ANALYSIS OF FISSION-INDUCED DIMENSIONAL*  
382 *CHANGES IN SINGLE CRYSTALS OF URANIUM*. Tech. Rep. ANL-5676, Argonne National  
383 Laboratory
- 384 Perdew, J., Burke, K., and Ernzerhof, M. (1996). Generalized gradient approximation made simple. *Phys.*  
385 *Rev. Lett.* 77, 3865
- 386 Perdew, J., Burke, K., and Ernzerhof, M. (1997). Erratum: Generalized gradient approximation made  
387 simple. *Phys. Rev. Lett.* 78, 1396
- 388 Schachinger, L. and Lamprecht, I. (1989). Heat capacity of uranium metal at low temperatures. a  
389 reminiscence. *Thermoc. Acta* 151, 203
- 390 Söderlind, P. (1998). Theory of the crystal structures of cerium and the light actinides. *Adv. in Phys.* 47,  
391 959
- 392 Söderlind, P., Grabowski, B., Yang, L., Landa, A., Bjorkman, T., Souvatis, P., et al. (2012). High-  
393 temperature phonon stabilization of  $\delta$ -uranium from relativistic first-principles theory. *Phys. Rev. B* 85,  
394 060301
- 395 Taylor, C. (2008). Evaluation of first-principles techniques for obtaining materials parameters of alpha  
396 uranium and the (001) alpha uranium surface. *Phys. Rev. B* 77, 094119
- 397 Timko, J., Bucher, D., and Kuyucak, S. (2010). Dissociation of nacl in water from ab initio molecular  
398 dynamics simulations. *J. Chem. Phys.* 132, 114510
- 399 Touloukian, Y., Kirby, R., Taylor, R., and Desai, P. (1975). *Thermophysical Properties of Matter - Thermal*  
400 *Expansion: Metallic elements and alloys*, vol. 12 (IFI/Plenu.)
- 401 Wang, C., Dai, Y., Gao, H., Ruan, X., Wang, J., and Sun, B. (2010). Ab initio molecular dynamics study of  
402 fe adsorption on tin (001) surface. *Mat. Trans.* 51, 2005
- 403 Xiang, S., Huang, H., and Hsiung, L. (2008). Quantum mechanical calculations of uranium phases and  
404 niobium defects in gamma-uranium. *J. Nucl. Mater.* 375, 113
- 405 Yoo, C.-S., Cyun, H., and Soderlind, P. (1998). Phase diagram of uranium at high pressures and  
406 temperatures. *Phys. Rev. B* 57, 10359